Proton acceleration in the electrostatic sheaths of hot electrons governed by strongly relativistic laser-absorption processes

S. Ter-Avetisyan,[1,*] M. Schnürer,[1] T. Sokollik,[1] P. V. Nickles,[1] W. Sandner,[1] H. R. Reiss,[1] J. Stein,[2,3,†] D. Habs,[3] T. Nakamura,[4] and K. Mima[4]

[1]*Max-Born-Institute, Max-Born-Strasse 2a, D-12489 Berlin, Germany*

[2]*Max-Planck-Institut für Quantenoptik, Hans-Kopfermann-Strasse 1, D-85748 Garching, Germany*

[3]*Ludwig-Maximilians-Universität München, Am Coulombwall 1, D-85748, Garching, Germany*

[4]*Institute of Laser Engineering, Osaka University, 2-6 Yamadaoka, Suita, Osaka 565-0871, Japan*

(Received 2 March 2007; revised manuscript received 14 September 2007; published 11 January 2008)

Two different laser energy absorption mechanisms at the front side of a laser-irradiated foil have been found to occur, such that two distinct relativistic electron beams with different properties are produced. One beam arises from the ponderomotively driven electrons propagating in the laser propagation direction, and the other is the result of electrons driven by resonance absorption normal to the target surface. These properties become evident at the rear surface of the target, where they give rise to two spatially separated sources of ions with distinguishable characteristics when ultrashort (40 fs) high-intensity laser pulses irradiate a foil at 45° incidence. The laser pulse intensity and the contrast ratio are crucial. One can establish conditions such that one or the other of the laser energy absorption mechanisms is dominant, and thereby one can control the ion acceleration scenarios. The observations are confirmed by particle-in-cell (PIC) simulations.

DOI: 10.1103/PhysRevE.77.016403 PACS number(s): 52.38.Kd, 41.75.Jv, 52.50.Jm

The absorption mechanisms of intense laser radiation are the basic processes in laser-matter interaction studies. At very high laser intensities, relativistic electron beams with tens of MeV kinetic energy and hot-electron populations will be created inside the target. There is considerable interest in the generation of energetic electrons due to its relevance to the fast ignitor concept [1].

Several mechanisms can produce high-energy electrons. For laser intensities higher than 10^{18} W/cm^2, electrons driven by the ponderomotive potential become relativistic. A characteristic parameter is the classical normalized momentum of electrons quivering in the laser electric field: $a = 8.53 \times 10^{-10} \lambda[\mu\text{m}]\ I^{1/2}\ [\text{W/cm}^2]$. At a laser intensity of 2×10^{19} W/cm^2, which is relevant to our experiments, a is approximately equal to 3, defining a strongly relativistic regime.

For $a > 1$, the effect of the laser magnetic field is no longer negligible, and the $e\mathbf{v} \times \mathbf{B}$ component of the Lorentz force couples with the electric force to drive the electrons in the laser propagation direction. At intensities of about 10^{19} W/cm^2 and an intensity contrast ratio of $1:10^{-8}$, it was shown that the electron temperature is dominated by the ponderomotive potential for those electrons directed along the axis of the laser beam. Temperatures of 1 MeV have been measured [2].

Another mechanism responsible for energetic electron production at the critical density n_c is resonance absorption, which occurs efficiently for p polarized radiation [3,4] at oblique laser incidence. These electrons create a smooth density and temperature profile in the interior region of the target, having a maximum in a direction normal to the target surface.

Thus the electrostatic sheath at the rear side of the target is built up either by electrons driven ponderomotively, or by resonance absorption. It is the sheath that accelerates the ions. Due to their directionality, one can separate them if the axis of the laser beam is not directed along the target normal. Recently we have shown that a second source of ions emitted in a direction normal to the target can appear if the laser incidence is at 45° [5]. The results were explained with the assumption that with high-contrast laser interaction, the ponderomotively driven electrons create the second source of ions in addition to the source created by the electrons driven through resonance absorption. Thus the ions are accelerated in the target-normal direction from two distinct sources. Earlier, the direction of fast electron generation was studied using photoneutron reactions in copper [6]. It was found that a (0.3–1.5) ns duration pedestal preceded the (1–1.5) ps main laser pulse, modifying the interaction so that for a small preplasma scale the electron beam is normal to the target, and for a relatively long preplasma case, the electron beam is in the laser propagation direction.

In this paper, we present results from the direct measurement of electron populations produced by strongly relativistic, short pulse and high-contrast laser pulses in a thin foil target, which are completely different in character from those produced by the acceleration conditions in [6]. At 45° laser incidence on the target, two clearly distinguishable branches of electron trajectories have been measured by Čerenkov diagnostics. This correlates with proton emission from two separated sources, which have been resolved with a high-spatial-resolution Thomson spectrometer. The crucial parameters of the experiment are the laser pulse intensity and the contrast ratio.

A particle-in-cell (PIC) simulation of the experimental parameters shows that the dominant electron acceleration pro-

*sargis@mbi-berlin.de

†Present address: DLR Institut für Technische Physik, Pfaffenwaldring 38-40, 70569 Stuttgart, Germany.

cess depends on the profile of the preplasma. For plasmas where the scale length of the preplasma is larger than the laser wavelength, a plasma wave is resonantly excited at the critical density surface, which results in the generation of fast electrons propagating in the target-normal direction [7]. If the preplasma scale length is smaller than the laser wavelength, a well-collimated electron beam is accelerated by ponderomotive forces in the propagation direction of the laser [8,9].

In the experiments, a 40 fs pulse from a multi-TW Ti: sapphire laser was focused onto a thin (6 μm) aluminum foil target at 45° with an intensity of about 2×10^{19} W/cm^2 [10]. The temporal contrast of the laser pulse was characterized by a scanning third-order cross correlator with a dynamic range of 10^{10}, having a resolution of 150 fs and a scanning range of ±200 ps. The pulse shape several ns before the main pulse was controlled by a fast photodiode with temporal resolution of about 300 ps. In typical operating conditions, the amplified spontaneous emission (ASE) pedestal of the laser pulse, several picoseconds before the pulse peak, was at a level of $(0.8-5)\times10^{-7}$ relative to the peak intensity. This is termed "low" contrast. The ASE pedestal could be reduced by driving the Ti: sapphire laser amplifiers in specific delayed pump modes. This led to a reduction of pulse energy by up to 550 mJ, but it permitted an improvement of the ASE level down to $(1-3)\times10^{-8}$, which is referred to as "high" contrast. In both cases, no prepulses were observed.

The Čerenkov method, applied as an electron diagnostic, uses the partial conversion of the electron bunch energy into a flux of photons in a medium where the electron velocity is higher than the light velocity [11]. A 50 μm tesa foil (polypropylene with chemical composition $(-C_3H_6-)_n$) used as a Čerenkov radiator was attached with a very thin layer of Acrylat glue to the target rear, and imaged with an objective ($f=8$ cm) and a magnification of about 15 to a gated charge-coupled device (CCD) camera. Due to its index of refraction of 1.49, and an insignificant fluorescence yield, this material is well suited as a Čerenkov medium. In addition, a 50 μm path length of this low Z substance has a negligible effect on the energy and main direction of the electrons. Propagating through the foil, the electron beam undergoes filamentation [12], but nonetheless with unaltered beam directions emerging from the target. To block any light from the laser pulse and its harmonics, a 6 mm Schott BG18 filter and a 3 mm VG8 filter were inserted into the beam path. These filters yield a spectral window centered at 510 nm with a half width of 70 nm. A weak and uniformly distributed background signal from transition radiation is emitted as a result (cf. [13]). For the medium and the geometry used, the detected Čerenkov light is associated with electrons in the 180–240 keV energy interval.

Measurements of the ion energies were carried out with a Thomson spectrometer [14]. In order to achieve high spatial resolution, we set up a Thomson spectrometer in a 1:12 imaging mode [15], providing spatial resolution of about 20 μm. This estimate takes into account the laminarity of the proton beam, and is measured from the spreading of a spectral trace that is a consequence of the divergence of the proton beamlet intercepted by a screen with a 30 μm pinhole.

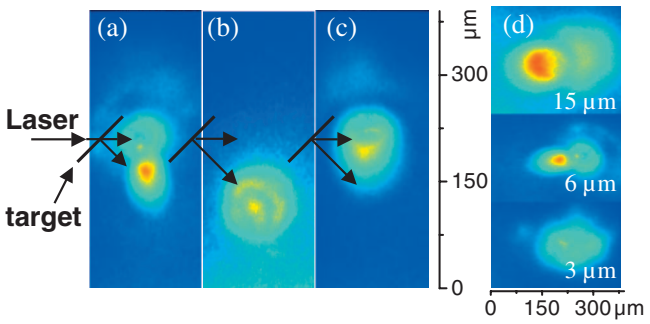

FIG. 1. (Color) Spatially resolved CCD pictures of Čerenkov radiation (arrows show emission direction) at 45° laser incidence resulting from electrons propagating: (a) In the laser direction and perpendicular to it; or (b) perpendicular to the laser direction only; and (c) in the laser direction only. (d) Recorded Čerenkov light distributions as a function of Al-target thickness. With a 3 μm target the two components are merged together, while at 6 μm they are clearly separated. When the target thickness is 15 μm, further broadening of the electron beams propagating inside the target occurs and blurs the Čerenkov emission.

The Čerenkov medium (tesa film) behind the target made it impossible to use both diagnostics simultaneously for the single laser shot. Therefore, correlations between the data sets are statistically relevant. Due to a 10 Hz repetition rate of the Ti: sapphire laser, and using on-line detection systems for both diagnostics, the statistical uncertainties could be minimized.

Figure 1 shows spatially resolved CCD pictures of Čerenkov radiation behind the 6 μm Al target at 45° laser incidence [(a)–(c)], and it shows the evolution of the Čerenkov signal as a function of target thickness (d). The arrows inserted in the pictures show the target irradiation and Čerenkov emission geometry. In the pictures, one of the two components of the hot electron current produced is identified as a consequence of hot electrons driven along the target normal due to resonance absorption, and the other component along the laser propagation axis is due to the ponderomotive force. Whereas, in Fig. 1(a) both electron components make a comparable contribution to the resulting Čerenkov emission, resonantly and ponderomotively driven electrons are dominant in Figs. 1(b) and 1(c), respectively. The appearances of the emission patterns are statistical, and correlated with the statistics of the laser pulse contrast shot-to-shot fluctuation data. Due to target alignment along the laser axis, the Čerenkov emission resulting from electrons propagating perpendicular to the target could be shifted [Fig. 1(b)] on the detector plane. The evolution of the Čerenkov signal as a result of target thickness is shown in Fig. 1(d). With a 3 μm target the two components are merged together, while at 6 μm they are clearly separated. When the target thickness is 15 μm, further broadening of the electron beams propagating inside the target occurs, and blurs the Čerenkov emission. The appearance of two electron components will be discussed further on the basis of PIC calculations (cf. below). In the experiments reported in Ref. [11], these two groups of separately moving hot electrons at the target rear side also were observed. Here we investigate the dynamics of the hot electron populations, and the consequences for the ion acceleration processes at

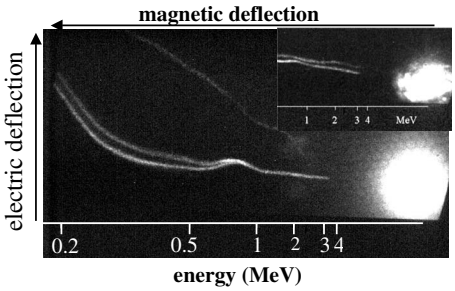

FIG. 2. CCD picture of a proton spectrum at 45° laser incidence on a 6 μm Al target, measured in the direction of the target normal. The inset shows proton spectra from a 3 μm target thickness at similar irradiation conditions. Two parallel proton parabolas show the existence of two sources of proton emission. The lower trace arises from the source created by electrons driven by resonance absorption, and the upper one from the source created by ponderomotively driven electrons.

"low" and "high" laser pulse contrasts. One can determine correlations between electron beam characteristics and ion acceleration features.

The resonantly and ponderomotively driven electron populations at the target rear side create two spatially separated electrostatic fields, from where the ions/protons can be accelerated. Therefore, one can expect ion emission from two spatially separated sources if the laser pulse contrast is between $10^{-8}-10^{-7}$, where both laser energy absorption mechanisms are equivalent. Indeed, the CCD picture of the proton spectrum in Fig. 2, measured in the direction of the target normal, shows two parallel proton parabolas, thus confirming the existence of the two sources of proton emission. The lower trace results from the source created by electrons from resonance absorption, and the upper one from the source created by ponderomotively driven electrons. The appearance of the second source (or second proton trace) is in good agreement with the detection of two electron populations by Čerenkov diagnostics [Fig. 1(a)]. This feature is never observed at normal laser incidence on the target. Figure 2 also shows that the parabolas are not perfect. This coincides with our previous findings [15] that the source position could be variable. Note that the two parallel traces in Fig. 2 change in a similar manner, while the proton spectrum of a 3 μm thick target (inset of Fig. 2) shows an independent character, which indicates complex source dynamics. The appearance of two proton traces also depends on laser intensity, because when the laser intensity decreases the ponderomotive acceleration plays a minor role, and the component in the laser propagation direction is not seen.

In order to see the differences in the electron acceleration processes and the implications for the following ion acceleration, we performed 2D-PIC simulations of laser irradiation onto targets with different scales of preplasma. The targets are 2 μm thick and have densities of 40 n_c. The preplasma is assumed to have an exponentially decreasing profile with two scale lengths. For the overdense region where the density is higher than 4 n_c, the scale length is 0.1 μm. For the lower density region resulting from an expanding corona plasma, the scale lengths are 0.3 μm for the small preplasma case and 3.5 μm for the large preplasma

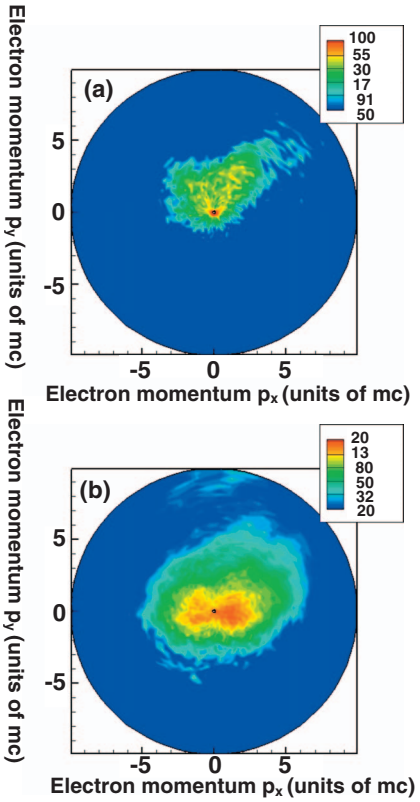

FIG. 3. (Color) Electron momentum distribution observed in PIC simulation at the target rear surface for the (a) "small" $L=0.3$ μm scale length preplasma case, and for the (b) $L=3.5$ μm "large" scale length preplasma case. Laser pulses irradiate the target from the left boundary. In the large preplasma case, resonance absorption plays the dominant role in accelerating electrons in the target-normal direction.

case. The initial electron temperature is 1 keV, and ions are kept immobile. The targets are irradiated by p-polarized laser pulses from the left boundary with wavelengths of 1 μm. The laser pulses ramp up in five laser cycles, and sustain a peak intensity of 2.0×10^{19} W/cm^2 that is uniform in the y direction. The pulse duration is 40 fs. The boundary conditions are absorbing in the x direction, and periodic in the y direction.

The differences resulting from the dominant acceleration processes are seen from the angular distribution of accelerated electrons. In Fig. 3, the angular electron momentum distributions observed in the PIC simulation at the target rear surface are shown for the (a) "small" $L=0.3$ μm scale-length pre-plasma case, and for the (b) $L=3.5$ μm "large" scale-length pre-plasma case. In the small preplasma case, ponderomotive acceleration and vacuum heating play dominant roles in energy absorption by electrons. Due to vacuum heating, laser energy is absorbed by low energy bulk electrons that are mainly accelerated in the target-normal direction. High energy electrons generated by ponderomotive acceleration propagate in the laser irradiation direction, and are reflected back toward the target at the specular angle, as can be seen clearly in the figure. For the large preplasma case, high energy electrons are mainly accelerated by resonance absorption in the target normal direction and are reflected back also

in the normal direction. These high energy electrons induce a strong magnetic field around the critical surface. In the small preplasma case, a magnetic field with uniform intensity is induced along the critical surface. This surface magnetic field prevents low energy electrons from propagating into the target, and makes them flow along the surface [16]. In the large preplasma case, a magnetic field is formed via a Weibel instability, which is in the target-normal direction. The surface field tends to make electrons flow along the surface, which leads to a uniform structure of the interaction surface. The target-normal magnetic field acts to collimate electron jets and return currents that are periodic along the surface. As a result, the critical density surface is rather smooth in the small preplasma case and modulated in the large preplasma case.

These different electron acceleration processes lead to differences in the lateral distributions of the rear side sheath field and proton acceleration as follows. The target size is 2 μm in thickness and 50 μm in width. The targets consist of 50% protons and 50% C^{4+}. Laser conditions are the same as above except that the laser pulses have a spot size of 15 μm with a super-Gaussian distribution. The boundary conditions are absorbing in the x and y directions. Ion density profiles at 150 fs after the pulse has ended are shown in Fig. 4. For the large preplasma case, the ion distribution is symmetric with respect to the laser axis passing through the laser focal point at the critical surface. Since a large part of the hot electrons propagate in the target-normal direction, the sheath field structure is similar to the normal incidence case. For the small preplasma case, however, the proton distribution is nonuniform and asymmetric. As is seen in previous simulations, very energetic electrons are accelerated in the laser propagation direction, and lower energy electrons are generated in the target-normal direction via vacuum heating. These two components result in two acceleration fronts of protons, which are clearly seen in Fig. 4(b) and detected in the experiment. The distance between the two acceleration points depends on target thickness and size of preplasma. In PIC simulation, the target is thinner and the density is lower than in the experiments. Thus the separation distance is considered to be larger than is visible in PIC simulation. Also, in Fig. 4 we show the angular distributions for preplasma scales of 0.3 and 3.5 μm in order to see clear differences, but similar results are seen at much smaller differences also. The important thing is that the dominant acceleration process changes when the scale length becomes smaller than the wavelength.

To summarize, in ultrashort (40 fs), high contrast, and strongly relativistic laser pulse interaction with thin foil targets, we observed two spatially separated electron populations when the laser is at oblique incidence. The ponderomotively driven electrons propagate in the laser propagation direction, and the electrons driven by resonance absorption propagate normal to the target surface. Correspondingly, protons are accelerated in a target-normal direction from two spatially separated sources. The laser intensity and the contrast determine the laser absorption process and thus they control the entire acceleration scenario. PIC simulations confirm these findings.

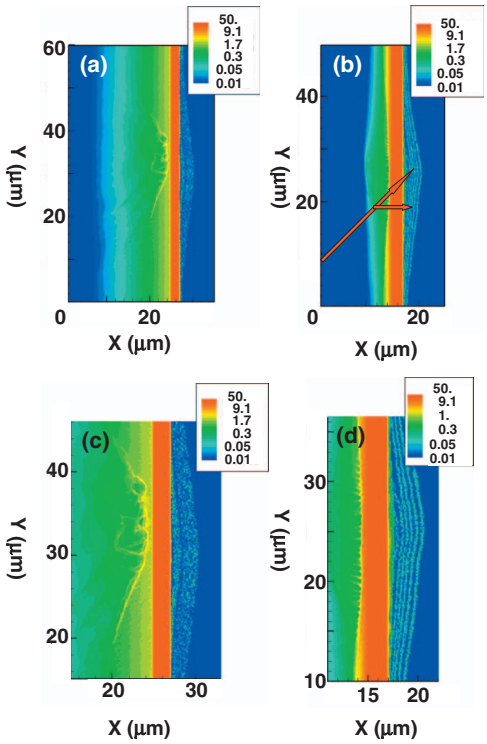

FIG. 4. (Color) Ion density distribution for a (a) large (L =3.5 μm) preplasma and a (b) small (L=0.3 μm) preplasma. Laser irradiation is from the left boundary, where the spot size is 15 μm, and the spot center corresponds to y=8.5 μm at the left boundary. Two arrows in (b) indicate the trace of the laser spot center and the target-normal projection of the spot center at the critical surface. Magnified figures around the laser focal point are plotted in (c) and (d) for large and small preplasma cases, respectively.

This work was partly supported by DFG–Sonderforschungsbereich Transregio TR18 and GK 1203 and performed under the grant-in-aid of Science Research Foundation No. 15GS0214, and the grant-in-aid for Young Scientists (B) No. 18740351.

[1] M. Tabak *et al.*, Phys. Plasmas **1**, 1626 (1994).
[2] G. Malka and J. L. Miquel, Phys. Rev. Lett. **77**, 75 (1996).
[3] F. N. Beg *et al.*, Phys. Plasmas **4**, 447 (1997).
[4] Z. Li *et al.*, Phys. Plasmas **13**, 043104 (2006).
[5] S. Ter-Avetisyan and P. V. Nickles, JETP Lett. **83**, 206 (2006).
[6] M. I. K. Santala *et al.*, Phys. Rev. Lett. **84**, 1459 (2000).
[7] K. Estabrook and W. L. Kruer, Phys. Rev. Lett. **40**, 42 (1978).
[8] W. L. Kruer and K. Estabrook, Phys. Fluids **28**, 430 (1985).
[9] S. C. Wilks, W. L. Kruer, M. Tabak, and A. B. Langdon, Phys. Rev. Lett. **69**, 1383 (1992).

[10] M. P. Kalachnikov *et al.*, Laser Phys. **12**, 368 (2002).
[11] J. Stein, E. Fill, G. Pretzler, and K. Witte, Laser Part. Beams **22**, 315 (2004).
[12] M. Manclossi, J. J. Santos, D. Batani, J. Faure A. Debayle, V. T. Tikhonchuk, and V. Malka, Phys. Rev. Lett. **96**, 125002 (2006)
[13] J. Stein, Ph.D. thesis, Ludwig-Maximilians-Universität, München, 2005 (unpublished).
[14] S. Ter-Avetisyan, M. Schnürer, and P. V. Nickles, J. Phys. D **38**, 863 (2005).
[15] J. Schreiber *et al.*, Phys. Plasmas **13**, 033111 (2006).
[16] T. Nakamura, S. Kato, H. Nagatomo, and K. Mima, Phys. Rev. Lett. **93**, 265002 (2004).